ISTITUTO NAZIONALE DI FISICA NUCLEARE

Laboratori Nazionali di Frascati

INFN-17-09/LNF(Thesis)
27th April 2017

# Time resolution of a Triple-GEM detector for future upgrade of the CMS muon system

Alice Alfonsi

Tutor Universitario
Emanuele Santovetti[1]

Tutor Aziendale
Luigi Benussi[2]

*[1]INFN-Sezione di Roma Tor Vergata Via della Ricerca Scientifica 1, Roma, Italy*
*[2]INFN-Laboratori Nazionali di Frascati Via E. Fermi 40, Frascati, Italy*

## Abstract

In this report results of the time resolution analysis of a GEM (Gas Electron Multiplier) detector prototype are discussed. This study was performed within the purview of an R&D activity regarding muon detectors for the CMS experiment, aiming at the future high luminosity upgrade of LHC, where a high-rate triggering for charged particles is needed. GEM chambers are particularly promising for this purpose, since they are able to handle the extremely high particle rates expected, especially in the muon forward region. The measurements were performed at the ASTRA facility of the INFN National Laboratory of Frascati (LNF). The study was accomplished by using cosmic muons, and by employing two different gas mixtures: Ar/CO2/CF4 (45%/15%/40%), and Ar/CO2 (70%/30%).

Pubblicato da SIDS–Pubblicazioni
Laboratori Nazionali di Frascati

# Contents

# Chapter 1

# GEM technology

## 1.1 GEM detectors

A GEM (Gas Electron Multiplier) detector is a particular type of MPGD (Micro-Pattern Gas Detector), originally proposed by F. Sauli in 1996, and nowadays employed in a large number of developments and applications [1–3]. The key features that led to its growing success are the large gain for moderate applied voltage, the high rate capability (greater than $5 \times 10^5$ Hz/mm$^2$), the gain uniformity and the robustness with respect to ageing processes and discharges [4]. Moreover, it has time resolution of the order of 5 ns.

A standard GEM consists of a thin (50 μm) Kapton[1] insulating foil, clad on each side with a 5 μm thick copper coating. The foil is chemically perforated to obtain a high surface density of holes, that are arranged hexagonally with a pitch of 140 μm. The holes exhibit a bi-conical structure arising from the perforation process, that employs standard photolitographic technologies [5]: the metal clad polymer is engraved on both sides with the desired hole pattern, and then a controlled immersion in a polymer-specific solvent opens the channels in the insulator. This leads to typical holes with an external diameter of 70 μm and an internal diameter of 50 μm, as depicted in Figure 1.1. Indeed, a thorough control of the etching conditions allows to obtain a nearly cylindrical shape, that reduces the charging-up of the Kapton. This effect consists of the accumulation of charges on the insulating surfaces, resulting in local changes of the electric field and thus affecting the amplification process [6]. Therefore, the charging-up reduction guarantees a more uniform gain.

The structure of a standard GEM detector is shown in Figure 1.2: the GEM

[1]Kapton® is a polyimide film developed by DuPont™, with a unique combination of electrical, thermal, chemical and mechanical properties that withstand extreme temperature, vibration and other demanding environments.

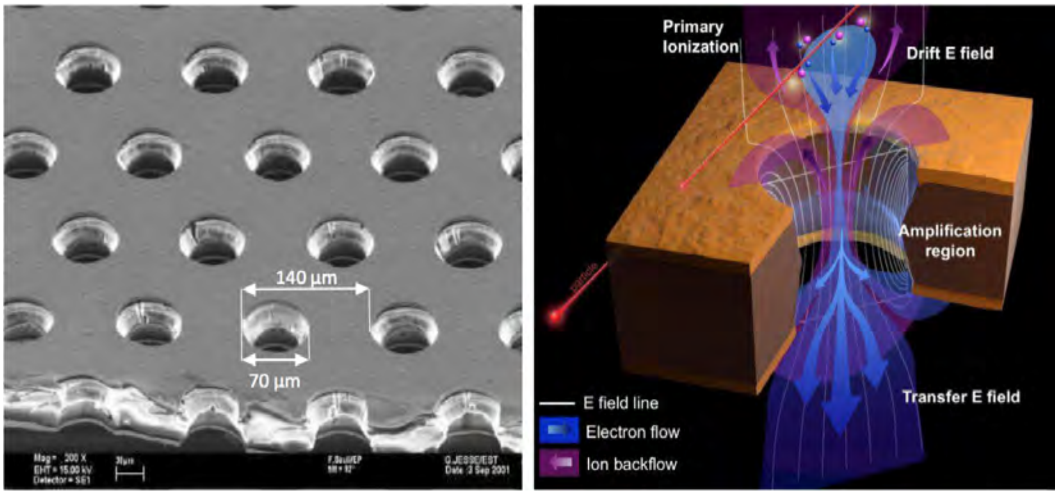


**Figure 1.1.** Left: Scanning Electron Microscope (SEM) picture of a GEM foil. Right: schematic view of the electric field lines (white), electron flow (blue) and positive ion flow (purple) through a GEM hole [7].

foil is inserted inside of the space between two flat parallel electrodes, which is filled with a gas mixture.

When a charged particle crosses the detector, ionisation electrons are produced in the drift gap, that is located between the cathode and the GEM foil. If a suitable voltage is applied on the electrodes, all the electrons released by gas ionization drift towards the GEM foil and into the holes, where they undergo a charge multiplication process. The GEM foil, thanks to its structure, exhibits in fact a high dipole field within the holes, that supplies the electrons with enough energy to start secondary ionisations, resulting in charge multiplication; the electric field lines are shown in Figure 1.1. Each hole works as an independent charge amplification channel, being screened from the neighbouring holes, and the multiplication occurs almost entirely within the holes. The gain is also insensitive to the foil shape.

The electrons resulting from charge amplification are released in the induction gap between the GEM foil and the anode, and drift towards the latter. The charge collection and readout anode can be patterned with strips or pads or some combination of the two, arranged in arbitrary shapes. Thanks to the absence of thin anodes, GEM detectors have a very high rate capability and are insensitive to radiation damage induced by polymerization[2] up to very high integrated fluxes [8]. This represent a great improvement with respect to other devices such as the Multi-Wire Proportional Chamber (MWPC), since the small

[2]Gas polymerization results in the production of granular solid polymers.

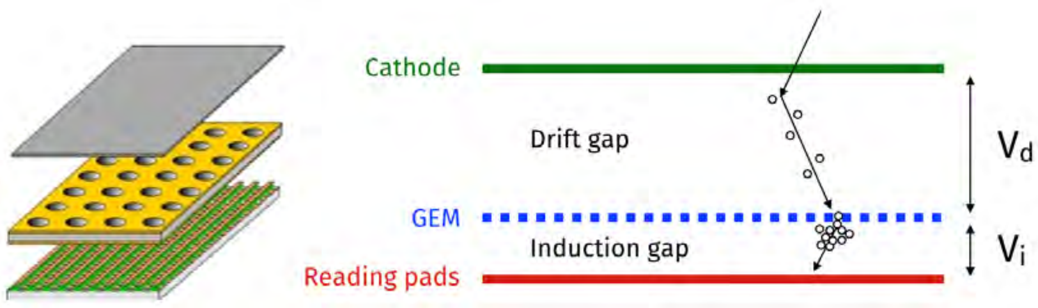


**Figure 1.2.** Left: 3D structure of a standard GEM detector [9]. Right: functioning scheme of a GEM detector.

area of anode wires make them particularly sensitive to the creation of thin insulating layers caused by the polymerization of organic gases or pollutants, resulting in fast ageing under irradiation [4].

Assuming a constant electric field, an electron spends a time $t_d = g_i/v_d$ to cross the induction gap, where $g_i$ is the gap size and $v_d$ is the electrons drift velocity. Assuming no cross-talk between adjacent pads, the signal induced on a pad by one electron is a current pulse of duration $t_d$ and intensity $I = e/t_d$. The total signal induced on a pad by a particle that crosses the GEM detector is the sum of the signals produced by every single ionisation electron, amplified by the multiplication through the GEM foil. Each one of these signals is delayed in time by the corresponding electron drift time in the drift gap, that varies with the coordinate where the electron is produced with respect to the cathode: an electron produced near the GEM foil needs less time to reach the foil than an electron produced near the cathode. This will be treated in detail in terms of time resolution in Section 1.3.

GEM based detectors have been tested with a wide variety of gas filling mixtures and operating conditions, including low and high pressures. Typically, a voltage difference of 350 V to 500 V is applied between the two copper sides of a GEM foil, producing an electric field as high as 100 kV/cm inside each hole, and resulting in an electron multiplication up to a few thousands. But the interesting feature of the GEM concept is that several GEM foils can be cascaded within the same detector, separated one from another by low field gaps. This allows to reach high gains while minimizing the discharge probability, since each element of the series can be operated at a much lower voltage than that needed to obtain a high gain with a single device. As shown in Figure 1.3, extensive tests demonstrated that an assemble of three cascaded GEM foils, the so called triple-GEM configuration, guarantees the reliability and breakdown

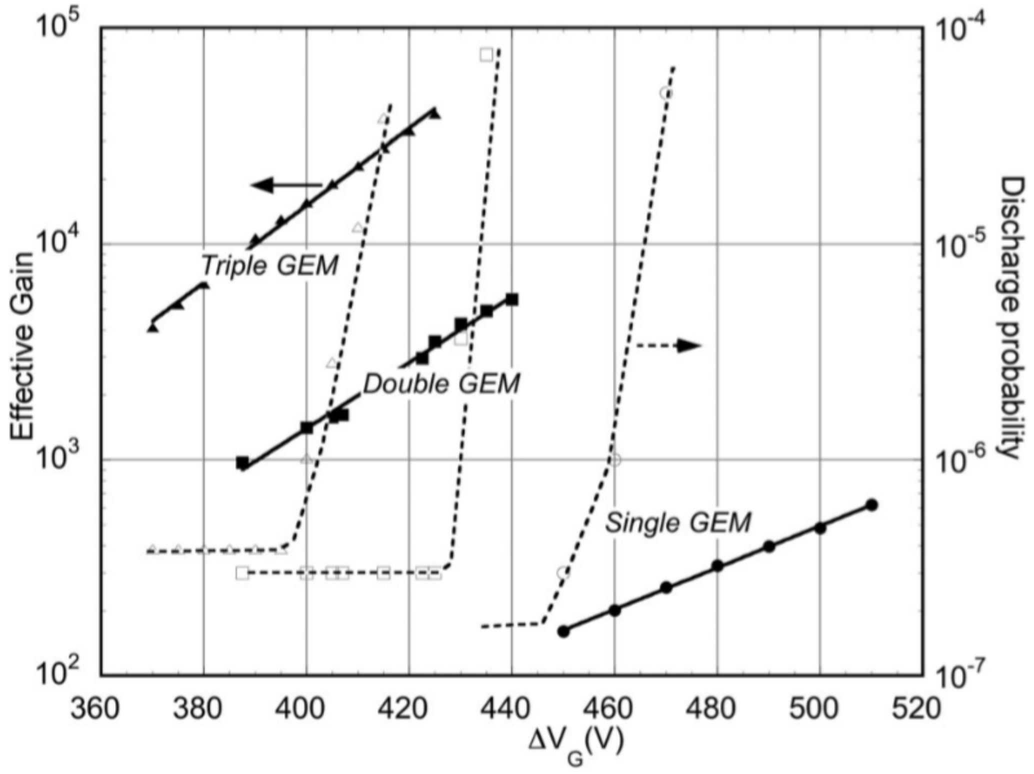


**Figure 1.3.** Gain (full lines) and discharge probability (dashed curves) of single, double and triple GEM detectors as a function of the individual GEM voltages [8].

suppression required in harsh beam conditions.

## 1.2 The Triple-GEM detector

A Triple-GEM detector, with its cross-section depicted in Figure 1.4, consists of three cascaded gas electron multiplier foils inserted in the space between two conductive plane electrodes, which is filled with an arbitrary gas mixture. The gaps dividing a GEM foil from another are called transfer gaps, and their purpose is to transport the secondary electrons produced in the holes of a foil towards the holes of the foil below.

A common choice for the size of the drift gap is 3 mm, large enough to minimise the inefficiencies in charged particle detection, but small enough to reduce the dead time due to pulse width. The first transfer gap size is usually set to 1 mm in order to reduce the so-called *bi-gem effect*: if this gap is large, a significant ionisation can be produced here, that is amplified by the subsequent two GEM foils and might then produce a detectable signal[3], resulting

[3]For example, a signal exceeding a discriminator threshold.

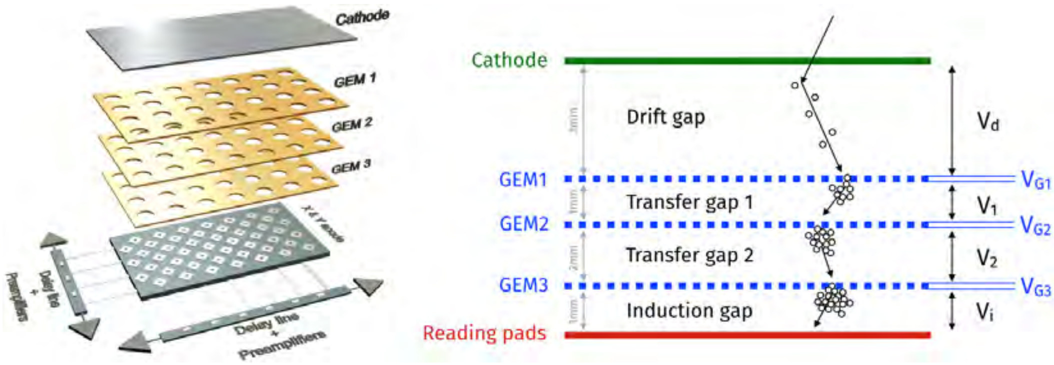


**Figure 1.4.** Left: 3D reconstruction of a typical Triple-GEM detector [10]. Right: functioning scheme of a Triple-GEM detector.

in hits early in time[4] with respect to the signals coming from the amplification of the charge deposited in the drift gap. This same effect cannot happen starting from the second transfer gap, since ionisation electrons produced there will only be amplified by the third GEM foil, and will be unlikely to produce a noticeable signal. The size of the second transfer gap is commonly set to 2 mm: this allows the increase of electron diffusion and of the number of holes of the third GEM foil involved in the multiplication process as well, reducing the discharge probability. Lastly, the induction gap size is 1 mm, small enough to increase the amount of charge integrated by the amplifier while avoiding discharges and gain non-uniformities.

By using a multi-channel voltage power supply, a chosen voltage difference can be applied in each gap and between the two copper sides of each GEM foil, creating high electric fields inside of them. The ionisation electrons produced in the drift gap cross the cascaded GEM foils and get multiplied three times. The total amplified charge then drifts in the induction gap towards the anode, giving rise to the induced current signal. As in the standard configuration, the anode can be segmented in reading pads, and connected to the readout electronics: this allows the Triple-GEM detector to be used also as a tracking detector.

## 1.3 Time resolution of a GEM detector

Summarizing broadly, a signal is produced when a charged particle passes through the detector, and a discriminator crossing on the signal rising edge gives the time of the track passing event.

[4] The signal from *bi-gem effect* will be anticipated of the quantity $\Delta t = g_t/v_d$, where $g_t$ is the width of the induction gap.

Travelling through the drift gap, this particle produces a series of primary ionisations, each one giving rise to a cluster[5] of following ionisation electrons. Therefore, the resulting rising edge of the signal at the amplifier input exhibits a stepwise profile, each step corresponding to the signal of a cluster (the time spread of electrons within the same cluster is much smaller than the time difference between clusters): the first step comes from the cluster produced closest to the first GEM foil, with the shortest arrival time.

The detector time resolution depends then on the statistics of the clusters produced in the drift gap. The space distribution of the cluster $j$ created at a distance $x$ from the first GEM foil is Poissonian:

$$P_j^n(x) = \frac{x^{j-1}}{(j-1)!} n^j e^{-nx}, \tag{1.1}$$

where $n$ is the average number of ionisation clusters per unit length. For a given electron drift velocity $v_d$, the distribution of the arrival times on the first GEM foil is

$$Pj(t_d) = P_j^n(v_d t_d), \tag{1.2}$$

that for the cluster produced closest to the first GEM foil ($j = 1$) becomes

$$P1(t_d) = n \cdot e^{-n v_d t_d}. \tag{1.3}$$

Therefore the intrinsic time resolution is $\sigma(t_d) = (n \cdot v_d)^{-1}$, assuming the ideal situation in which the first cluster is always triggered. This shows the importance of a high primary ionisation (high $n$) and a fast gas mixture (high $v_d$) in improving the time performance.

Nevertheless, the intrinsic time resolution represents only a lower limit: in real situations, the limited collection efficiency of the first GEM foil, the statistical fluctuations of the gas gain and the finite threshold of the electronics must be taken into account, leading to a possible failure in the detection of the $j = 1$ cluster. Since the other ionisation clusters have a probability distribution with larger $\sigma(t_d)$ than the $j = 1$ cluster (but still proportional to $n^{-1}$), the maximisation of the detection efficiency of the $j = 1$ cluster is a determining factor in the time resolution of a GEM detector. The use of a fast gas mixture ensures a large collection efficiency and helps obtaining a high detection efficiency.

[5] A cluster is defined as an ensemble of electrons produced after a primary ionisation, whose spatial spread is of the order of 100 μm around the primary ionisation point.

# Chapter 2

# Compact Muon Solenoid

## 2.1 CMS detector

CMS, acronym for Compact Muon Solenoid, is a general purpose detector at the Large Hadron Collider, that makes use of proton-proton collisions to investigate a wide variety of physics phenomena [11]. It is located in an underground cavern about 100 m deep near the french village of Cessy, corresponding to the interaction region number 5 (IR5) of the LHC ring.

The detector is built hermetically around the nominal collision point of the two counter-rotating proton beams of LHC. It exhibits a cylindrical symmetry with respect to the beam pipe: its structure can be split in a central cylindrical part, referred to as the barrel, and two endcap regions that encase the barrel transversally, one on each side. Overall, CMS benefits of a length of 21.6 m, a diameter of 15 m and a weight of about 14000 t, being the heaviest particle detector at colliders worldwide.

As shown in Figure 2.1, the detector consists of a series of subsystems, assembled in layers with different functionalities. The distinctive feature is the superconducting solenoid magnet located at its centre: it has an inner diameter of 5.9 m, and is capable of generating a magnetic field of up to 4 T[1]. Within the magnet there are the inner tracking system, which is closest to the interaction point, and the electromagnetic (ECAL) and hadron calorimeters (HCAL), that fill the space around the tracker. Outside of the magnet there is an extensive muon system, made up of layers interleaved in a steel yoke that sustains the entire structure. The yoke serves also as a hadron absorber for the muon system. It increases the field homogeneity in the tracker, and reduces the stray field by returning the magnetic flux to the solenoid. Additionally, forward muon

[1] Although the magnet is nominally designed to reach a 4 T axial magnetic field, it is operated at 3.8 T to preserve it while studying its behaviour and ageing.

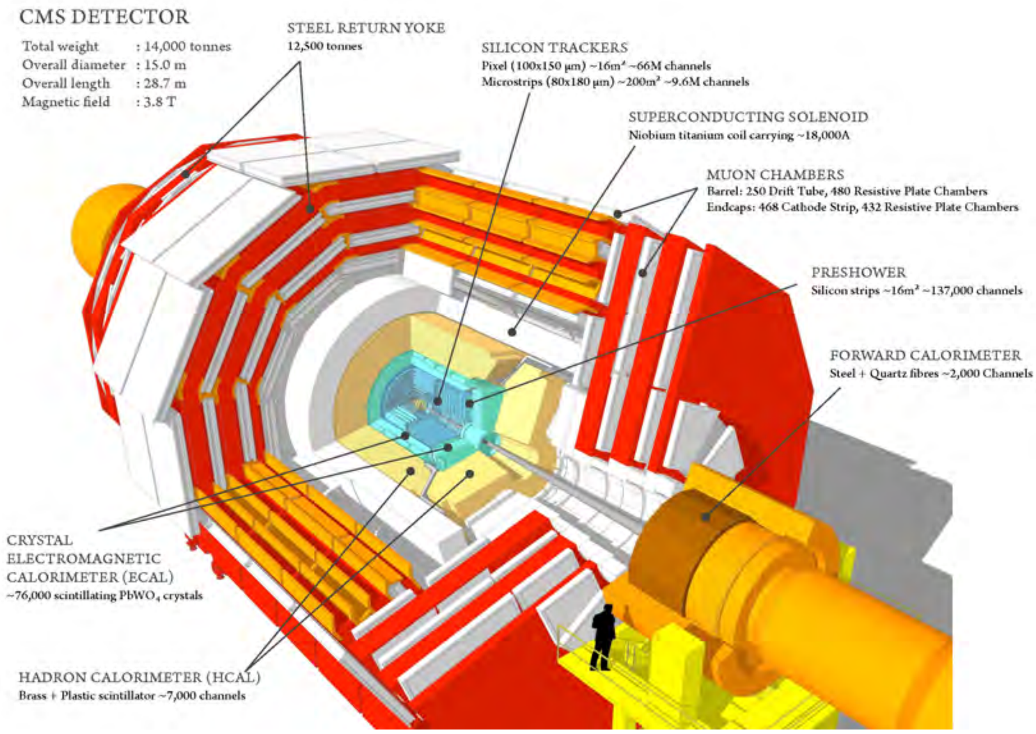


**Figure 2.1.** Cartoon of CMS outlining the various subsystems of the detector [CERN].

calorimeters are located after the endcap muon chambers, along the beamline.

## 2.2 Muon System

The CMS muon system [12] has three main purposes: muon identification, muon momentum measurement and muon triggering. In order to achieve these goals, three different gaseous detectors are used in an appropriate combination: Drift Tubes (DTs), Cathode Strip Chambers (CSCs) and Resistive Plate Chambers (RPCs).

DTs and CSCs provide a precise tracking of the muon particle: muon momentum and charge measurements are then obtained, thanks to the bending of the charged particle tracks inside of the magnetic return field (whose intensity goes from around 1.8 T in the barrel to 2.5 T in the endcaps). Muon identification is guaranteed by the amount of material within the solenoid and in the return yoke of the magnet, that ensures shielding from charged particles other than muons: the total material depth that a particle has to cross before reaching the end of the muon system is at least 20 interaction lengths for low pseudorapidities.

On the other hand, both the RPCs and the system based on DTs and CSCs

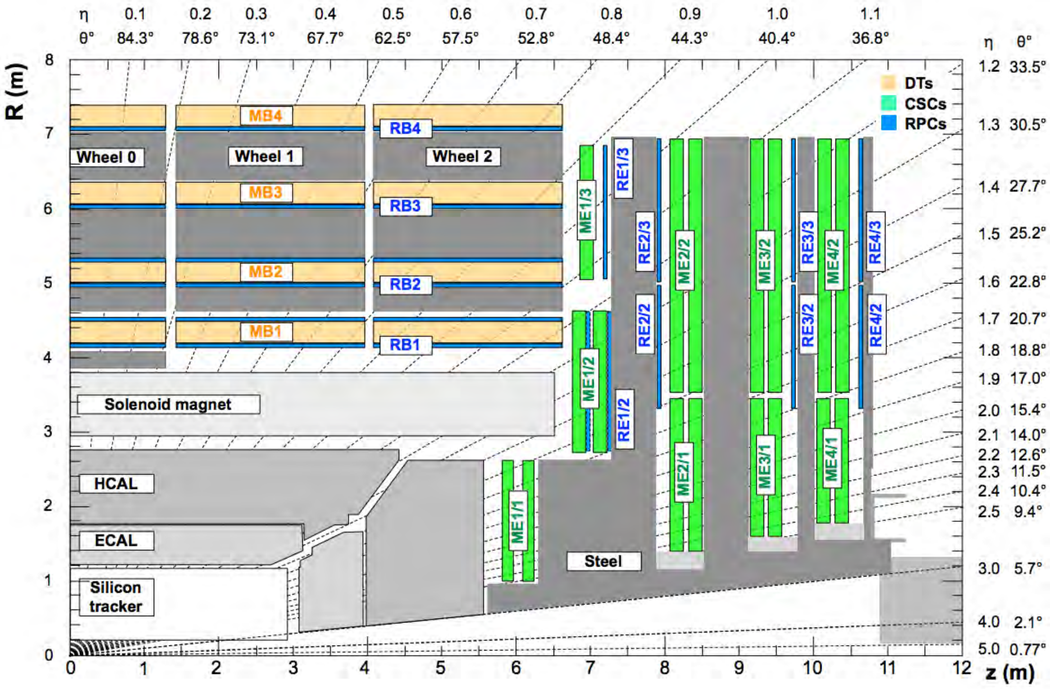


**Figure 2.2.** Layout of a quadrant of the CMS muon system afer the LS1 upgrade, in the $R - z$ plane with $z$ parallel to the beam and $R$ increasing upwards. Steel disks are shown as dark grey areas. DTs are in light orange, CSCs in green and RPCs in blue. From [13].

work independently to provide a redundant muon trigger: RPCs, thanks to their excellent time resolution, guarantee fast triggering, while DTs and CSCs give a good efficiency and purity.

Most of the muon system, which is shown in Figure 2.2, was installed in 2007, while major upgrades have been carried out in 2013-2014 during the first LHC Long Shutdown. The spectrometer consists of a cylindrical barrel section and two planar endcap regions supported by the rings of the steel return yoke. The detectors are organized in independently-operating modules called chambers, and the chambers are arranged in layers, referred to as muon stations, around a fixed value of $r$ (in the barrel) or $z$ (in the endcaps). There are four stations in the barrel region and in each endcap region. The return yoke plates interleave them, guaranteeing a sufficient thickness of iron to isolate electromagnetic showers that are produced due to muon bremsstrahlung between the stations.

The momentum resolution of the muon system is essentially determined by the muon bending angle at the exit of the solenoid coil. On the other hand, it may be degraded by the amount of material that the muon has to cross before reaching the first station, due to multiple scattering processes. These processes dominate up to $p_T$ values of 200 GeV/c, and the corresponding muon momentum resolution is $\sim 8\% - 15\%$ for small values of $|\eta|$. At higher momenta, the spatial resolution of the chambers starts to dominate, leading to a resolution of $20\% - 40\%$ at $p_T \sim 1$ TeV/c, depending on $|\eta|$.

The magnetic return field inside the iron yoke, together with the expected radiation flux, sets the environment in which the detectors must operate. In the barrel region, where the muon rate is moderate, the neutron-induced background is small and the return magnetic field is uniform, DTs are employed, covering a pseudorapidity range up to $|\eta| < 1.2$. In the endcaps, where the muon rates and the background levels are higher and the magnetic field is intense and non uniform, CSCs are employed, covering the pseudorapidity range $0.9 < |\eta| < 2.4$. RPCs are used in both the barrel and the endcap regions, up to $|\eta| = 1.8$[2]. In total, the muon system contains more than 25000 $m^2$ of active detection planes, and nearly 1 million electronic channels.

This system is highly affected by its alignment, both internal and with respect to the inner tracker. A misalignment can derive from imperfect assembly, temperature instabilities or deformations related to the magnetic field. Since muon measurements combine data from the tracker and from the muon chambers, it is crucial to accurately monitor the alignment of the spectrometer. This is done by means of a dedicated optical Muon Alignment (MA) system.

### 2.2.1 DT system

The barrel muon system is divided in 5 wheels along $z$, and every wheel is segmented in 12 $\phi$ sectors, each covering a 30° azimuthal angle. In each sector there are 4 muon chambers per wheel, forming muon stations at radii of ap-

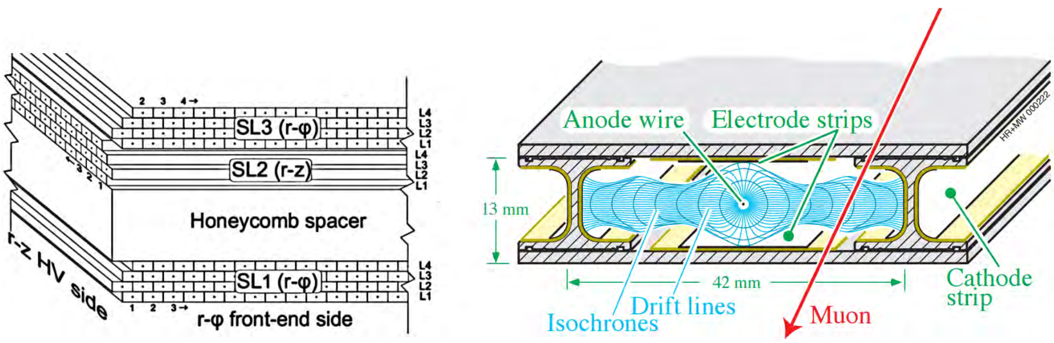


**Figure 2.3.** Left: Schematic view of a DT chamber, in which three superlayers are visible, as well as the honeycomb spacer. Right: Section of a drift tube cell. Taken from [15].

[2]The region $|\eta| < 1.8$ was covered during the LS1 upgrade of CMS. Before, only the first three endcaps disks were equipped with RPCs [14].

proximately 4.0 m, 4.9 m, 5.9 m and 7.0 m from the beam axis, labelled as MB1, MB2, MB3 and MB4 respectively.

A DT muon chamber is made of a number of superlayers (SLs), each consisting of 4 layers of drift tubes staggered by half a cell, to eliminate dead spots in the efficiency. A schematic view is shown in Figure 2.3 (left). Chambers of the first three stations employ 3 SLs, the two innermost measuring the muon position in the $r - \phi$ plane thanks to wires parallel to the beam line, and the outermost detecting the $z$ coordinate with orthogonal wires. The MB4 station lacks the $z$ measurement superlayer. An aluminium honeycomb structure is placed between the SLs to provide a lever arm for the track reconstruction. The longitudinal size of the chambers is limited by the segmentation of the barrel yoke, leading to a dimension of about 2.5 m. On the transverse side, the length varies among the stations, ranging from 1.9 m for MB1 to 4.1 m for MB4.

The individual drift tubes used throughout the system are rectangular cells with transverse size of $42 \times 13$ mm$^2$, that use a 85%/15% of $Ar/CO_2$ gas mixture, providing good quenching properties and a saturated drift velocity of about 55 $\mu$m/ns. A section of these detectors is shown in Figure 2.3, right. At its center each cell employs a 50 $\mu$m diameter gold-plated stainless-steel anode wire, that operates at a voltage of +3600 V. On the side walls of the tube there are two electrodes, and two more are located above and above the wires, in order to shape the effective drift field.

### 2.2.2 CSC system

Similarly to the barrel arrangement, there are four CSC muon stations integrated into each endcap yoke, referred to as ME1, ME2, ME3 and ME4. The stations are divided into rings, 3 for ME1 and 2 for the others, that are labelled MEi/n, where the integer $i = 1 - 4$ is the station index and $n$ decreases with the radial distance from the beam line.

The CSCs are multi-wire proportional chambers of trapezoidal shape positioned perpendicularly to the beam line, that can operate at high rates and in large non-uniform magnetic fields using a 40%/50%/10% mixture of $Ar/CO_2/CF_4$. As shown in Figure 2.4, they comprise 7 trapezoidal cathode panels each, interleaved by 6 gaps corresponding to planes of sensitive anode wires, running in the azimuthal direction. Every panel contains 80 cathode strips, each one subtending a constant $\phi$ angle between 2.2 mrad and 4.7 mrad. The anode wires have a diameter ranging from 30 $\mu$m in ME1/1 to 50 $\mu$m everywhere else, and a spacing of 3.16 mm to 3.12 mm (or 2.5 mm in ME1/1). All the chambers,

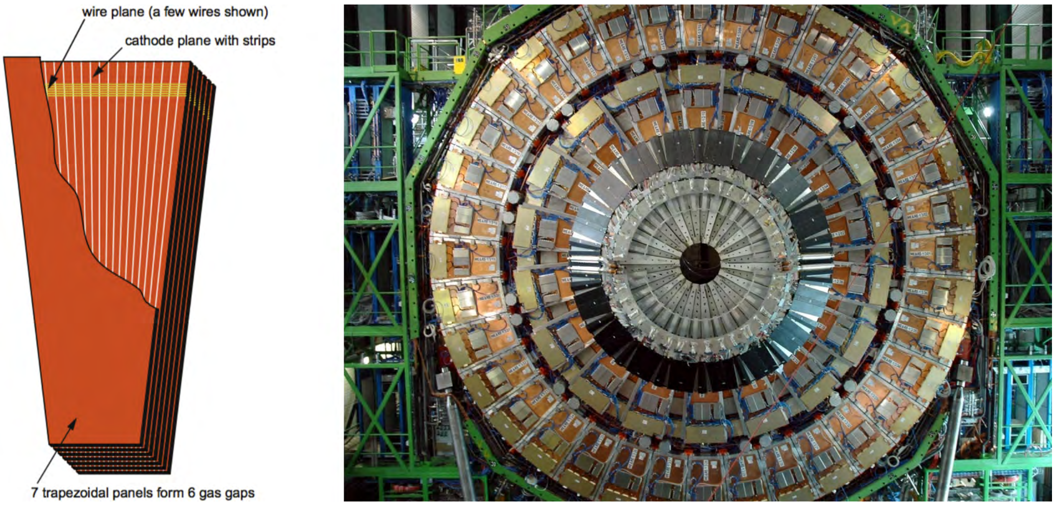


**Figure 2.4.** Left: Layout of a CSC, in which only a few wires are shown to indicate their azimuthal direction. Right: Photography of a completed ME1 station. From [11, 16].

except for the ME1/3 ring, overlap and provide contiguous $\phi$ coverage. They have different dimensions within the system, ranging in length from about 1.7 m to 3.4 m in the radial dimension. All the CSCs subtend a $\phi$ angle of about $10^{\circ}$ in the radial dimension, except for the inner rings of stations 2, 3 and 4, that subtend an angle of about $20^{\circ}$.

During the Run-1, the number of CSCs included in the system was 468. This number was increased with the LS1 upgrade, reaching a total of 540 chambers. The overall area covered by the sensitive planes of all the chambers is about 5000 $m^2$, the gas volume is larger than 50 $m^3$ and there is a total number of wires of about 2 million.

### 2.2.3 RPC system

Thanks to its fast response the RPC system provides an independent and dedicated trigger, complementary to that provided by CSCs and DT chambers, and with a looser $p_T$ threshold. Recalling the arrangement of the DTs, 6 layers of RPC chambers are embedded in the barrel iron yoke: 2 attached to the inner and outer side of the first two DT stations, providing redundancy, and 1 in each of the two last stations. The readout of the chambers is divided in 2 or 3 $\eta$ partitions called rolls. In the endcaps, there are 4 layers of RPCs arranged in 4 disks: RE1, RE2, RE3 and RE4. Each disk is composed of 2 concentric rings, labelled REn/2 and REn/3, where the integer $n = 1 - 4$ indicates the disk index. The CMS RPC basic module, shown in Figure 2.5, consists of 2 gaps, referred to as the up and the down gap, operated in avalanche mode with common

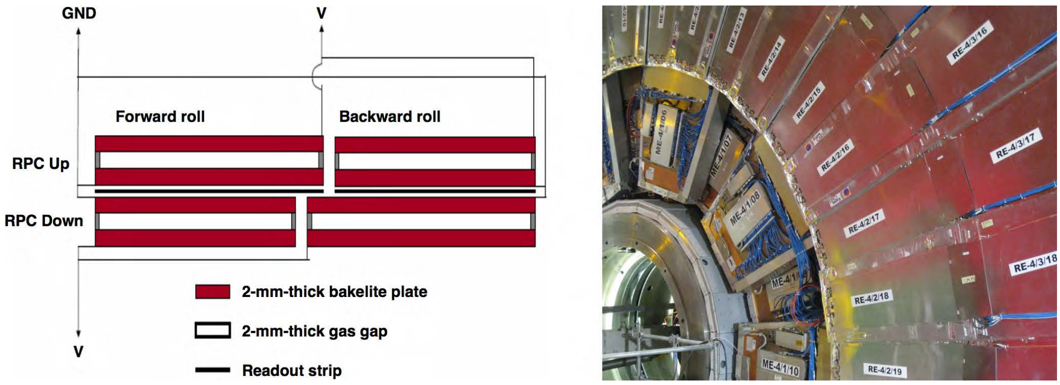


**Figure 2.5.** Left: Schematic view of a generic barrel RPC with two rolls. Right: Photography of endcap RPCs during the LS1. From [15, 17].

pick-up readout strips between them. This ensures reliable operation at high rates. Each gap consists of two 2 mm thick resistive Bakelite plates, separated by a 2 mm thick gas gap. The gas mixture used consists of 95.2% $C_2H_2F_4$, 4.5% isobutane and 0.3% $SF_6$. The outer surface of the Bakelite plates is coated with a thin conductive graphite layer, and a voltage of about 9.6 kV is applied. The total induced signal is the sum of the two single-gap signals. This allows the single gaps to operate at lower gas gains, with an effective detector efficiency higher than that of a single gap.

## 2.3 CMS muon system upgrade

The future upgrades planned for the LHC machine aim at achieving higher peak and integrated luminosities, well above those for which CMS was originally designed. In particular, a high luminosity upgrade is foreseen during a third long shutdown (LS3), that will take place in 2023. The high luminosity data taking period following LS3 is referred to as HL-LHC, or Phase-II: in the proposed scenario the instantaneous luminosity will reach $5 \times 10^{34}$ cm$^{-2}$s$^{-1}$, and 250 fb$^{-1}$ will be delivered per year, for 10 years of operation.

In order to cope with this expected harsh environment, the CMS muon system requires an upgrade too: the main challenges to face are radiation damage to the CMS sub-detectors due to the high integrated luminosity, and a very high pile-up that comes from the high instantaneous luminosity. This, especially in the forward region, will lead to a potential degradation of muon triggering and reconstruction [14].

The proposed Phase-II plan for the muon system, as shown in Figure 2.6, comprises: (i) the upgrade of existing detectors and associated electronics, to

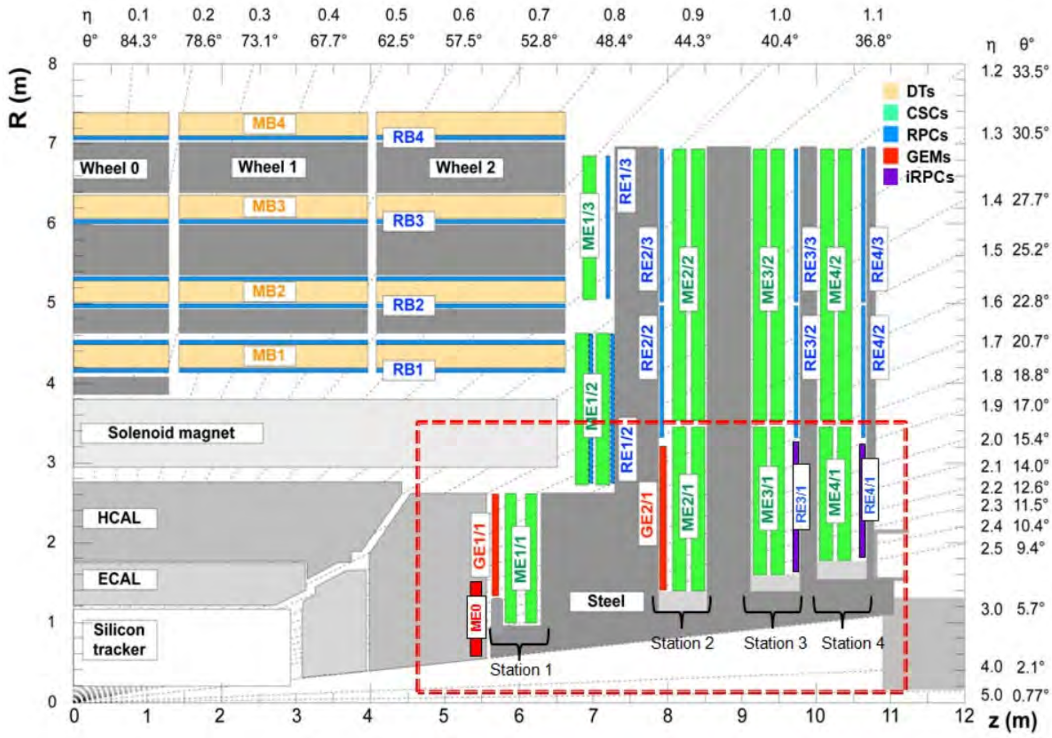


**Figure 2.6.** Layout of a quadrant of the CMS muon system afer the LS1 upgrade, in the $R - z$ plane with $z$ parallel to the beam and $R$ increasing upwards. Steel disks are shown as dark grey areas. DTs are in light orange, CSCs in green and RPCs in cyan. Additionally, the new forward muon detectors for Phase-II are shown within the red box: GEM stations (ME0, GE1/1, GE2/1) are in red, and improved RPC stations (RE3/1, RE4/1) are in blue. The interaction region is at the lower left corner. Taken from [19].

ensure their longevity and good performance; (ii) the installation of additional detectors in the region $1.6 < |\eta| < 2.2$, for redundancy and enhancement of trigger and reconstruction capabilities; (iii) the extension of coverage up to $|\eta| = 3$, to take advantage of the planned pixel tracking coverage extension.

The first two muon layers in the $1.6 < |\eta| < 2.2$ pseudorapidity region will be equipped with Triple-GEM detectors denoted by GE1/1 and GE2/1, while the third and fourth muon layers will be equipped with iRPC (improved RPC) detectors, denoted by RE3/1 and RE4/1. On the other hand, the extension to $|\eta| = 3$ will be achieved by installing an additional Triple-GEM detector, denoted by ME0 [18].

Triple-GEM detectors, thanks to their spatial ($\sim 100$ μs) and time ($5 - 8$ ns) resolution, their high efficiency ($> 98\%$) and their rate capability ($\sim 1$ MHz/cm$^2$), represent a feasible solution for the critical forward regions. The implementation of GE1/1 and GE2/1, whereas recovering redundancy in the forward region (where there is currently only CSCs coverage), will guarantee a better bending angle measurement, using the lever arm formed by the GEMs and the CSCs. This will greatly improve the transverse momentum resolution, allowing to discriminate between muons and low transverse momentum background, and therefore improving the trigger rate [20]. On the other hand, the ME0 is expected to supply good muon identification in offline analyses, taking advantage of the extensions of the rest of CMS (tracker and calorimeter).

# Chapter 3

# Experimental setup and measurements

## 3.1 Experimental setup

The experimental setup is shown in Figure 3.1 (left). It comprises a multi-channel voltage power supply, a fast high-sampling (10 GS/s) digital oscilloscope, a gas mixer system with environmental sensors and gas-chromatography, two paddle plastic scintillators and a Triple-GEM detector, with its associated front-end electronics.

The oscilloscope produces a large number of raw output files, each one containing the full information about a given recorded signal, in terms of the coordinates of each point that composes the signal in the $(\mathtt{time}, \mathtt{amplitude})$ space.

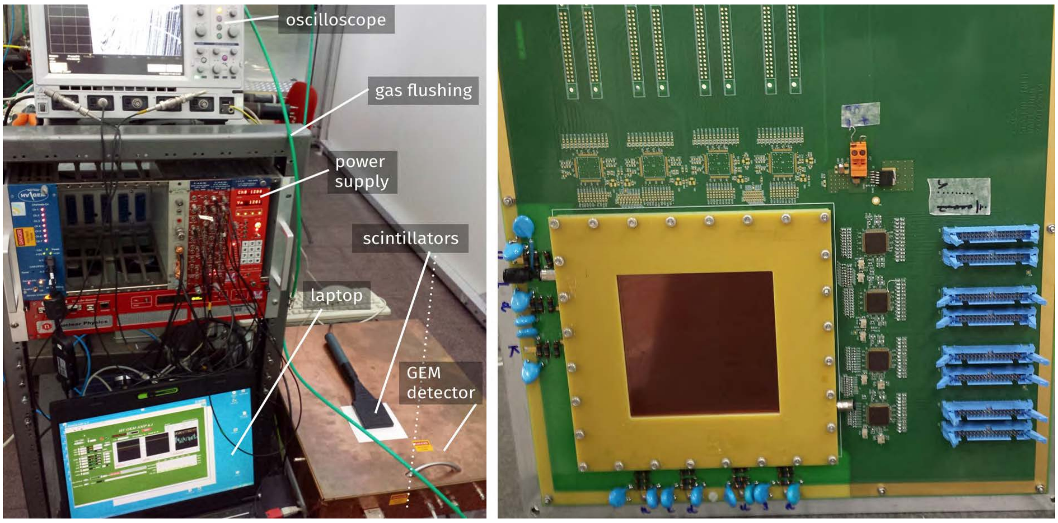


**Figure 3.1.** Left: photography of the experimental setup used. Right: readout PCB for the Triple-GEM detector.

The scintillators couple provide the trigger, needed to assure that the detected signal is produced by the crossing of a cosmic muon through the entire setup. The first scintillator is located on top of the Triple-GEM detector, and the second one is at the bottom. The trigger is given by the coincidence of both the devices, and the signal of the bottom one sets the start of the time measurement.

The Triple-GEM detector used has an active area of $10 \times 10\ \text{cm}^2$ and employs the standard gap configuration described in Section 1.2. Its readout board, as shown in Figure 3.1 (right), is equipped with GASTONE (GEM Amplifier Shaper Tracking ON Events) analog chips, that are low-noise and high-gain amplifiers [21]. Only one half of the detector is properly equipped with GASTONE chips and has then been used, but this does not affect time measurement results, since no tracking is required.

Two different gas mixtures have been employed to fill the space between the electrodes, obtaining two different sets of measurements: $Ar/CO_2/CF_4$

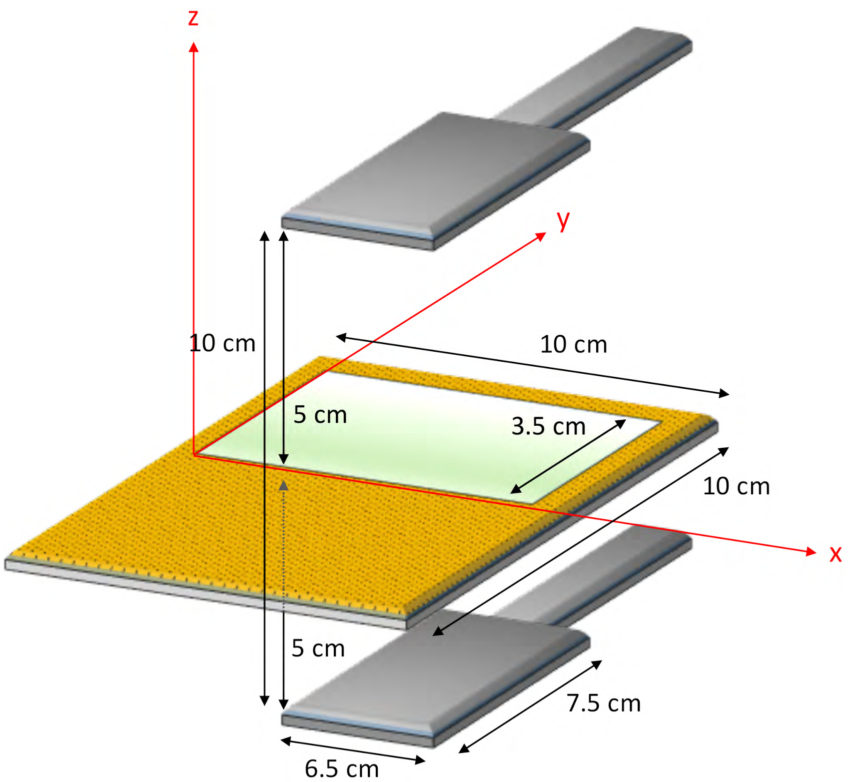


**Figure 3.2.** 3D reconstruction of the geometry of the detection system. The scintillator paddles are in grey, the GEM detector is shown in yellow, and the active area actually equipped with GASTONE chips is coloured in green. The coordinate system is marked in red.

(45%/15%/40%) and $Ar/CO_2/CF_4$ (70%/30%). In both mixtures, the primary gas in which ionization takes place is argon (Ar). As a noble gas, it can only be excited through the absorption or emission of photons, and allows to obtain avalanche multiplication of the primary ionization at much lower fields than that required by other molecules. Among noble gases, Ar is the best choice since it has a high specific ionization and is cheap. This reduces the discharge probability, improving the gain. A small fraction of both mixtures consists of carbon dioxide ($CO_2$), that acts as a quencher. In fact, being a polyatomic molecule, it undergoes radiationless transitions thanks to its rotational and vibrational nature. These transitions allow to dissipate part of the incident energy without emitting additional photons. The results is a very efficient ion exchange and the suppression of secondary effects, such as photon feedback and field emission. Therefore, $CO_2$ allows to get a stable gain, independent from the electronic noise. Overall, mixtures of Ar and $CO_2$ are fast for tracking and triggering applications. Moreover, a small quantity of tetrafluoromethane ($CF_4$) is added to the second mixture in order to improve the time performance of the detector: it is a fast and high average atomic number gas, and is frequently chosen among other similar molecules because it is non-flammable, non-corrosive, non-toxic, and shows a good compatibility with most of the metals, plastics and resins used in gaseous detectors construction.

## 3.2 Measurements and data analysis

The measurements have been carried out using cosmic muons, that are produced when cosmic rays collide with nuclei in the Earth's upper atmosphere. For each gas mixture, experimental data have been collected in a number of $\sim$ 24 h runs, each one at a fixed value of the voltage difference applied to the GEM foils, $V(GEM)_i$. In total, the measurement included five runs with the $ArCO_2CF_4$ mixture, at $V(GEM)_i$ values of $(430, 440, 450, 460, 470)$ V, and four runs with the $ArCO_2$ mixture, at $V(GEM)_i = (370, 380, 390, 400)$ V. The chosen $V(GEM)_i$ ranges were constrained by the request of a sufficient primary ionization on one hand, and the need of avoiding discharges on the other.

Operationally, the time resolution estimation has been performed by collecting a large number of triggered muon signals, and studying the distribution of their arrival times, where the arrival time of a muon event is obtained using an offline simulated double threshold discriminator, in order to have more control over the data.

The analysis strategy involved five main steps, that will be discussed in the next sections. First, the two thresholds of the discriminator have been properly chosen. Then, the baseline of each triggered signal has been corrected in order to reduce the electromagnetic noise potentially degrading the measurements. The estimation of the time resolution as a function of the voltage applied to the GEM foils was thus carried out, followed by the study of the detector efficiency needed to appropriately compare the time performance of the two different mixtures. Finally, it was possible to estimate and compare the time resolution of the detector as a function of the efficiency, for the two gas mixtures.

### 3.2.1 Choice of discriminator thresholds

The two discriminator threshold values are meant to optimise the signal-to-noise ratio. The low threshold provides time information. It must be set really close to the estimated noise values, to ensure the crossing at the very beginning of the rising edge of the signal. This minimizes the *amplitude walk effect*, that is the dependence of the discriminator crossing on the signal amplitude: in fact, assuming a similar shape for all the signals, higher amplitudes generally imply shorter crossing times, and vice-versa. This effect is clearly visible comparing the two plots shown in Figure 3.3. On the other hand, the high threshold identifies the signal, reducing the noise contribution: the time measured thanks to the low threshold is recorded only if, within a given time delay, the high threshold is passed; this ensures that the measurement is performed on the rising edge of an effective signal, rejecting the fake time measurements due to noise crossing the low threshold. The delay is defined as $\Delta t = t_{low} - t_{high}$,

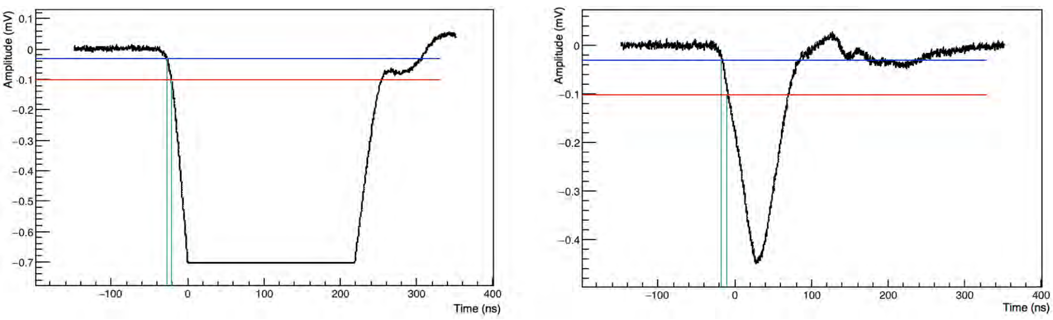


**Figure 3.3.** Chosen thresholds values for the offline simulation of a double threshold discriminator. Two representative signals are shown among the entire set of reconstructed oscilloscope samples. The blue solid line indicates the low threshold value, while the red line represents the high threshold. The two vertical cyan lines are the times at which the signal crosses the low and the high threshold, respectively. The difference on their position gives the delay $\Delta t$ between the two crossing times. The *amplitude walk effect* is also visible by comparing the arrival times of the two plots.

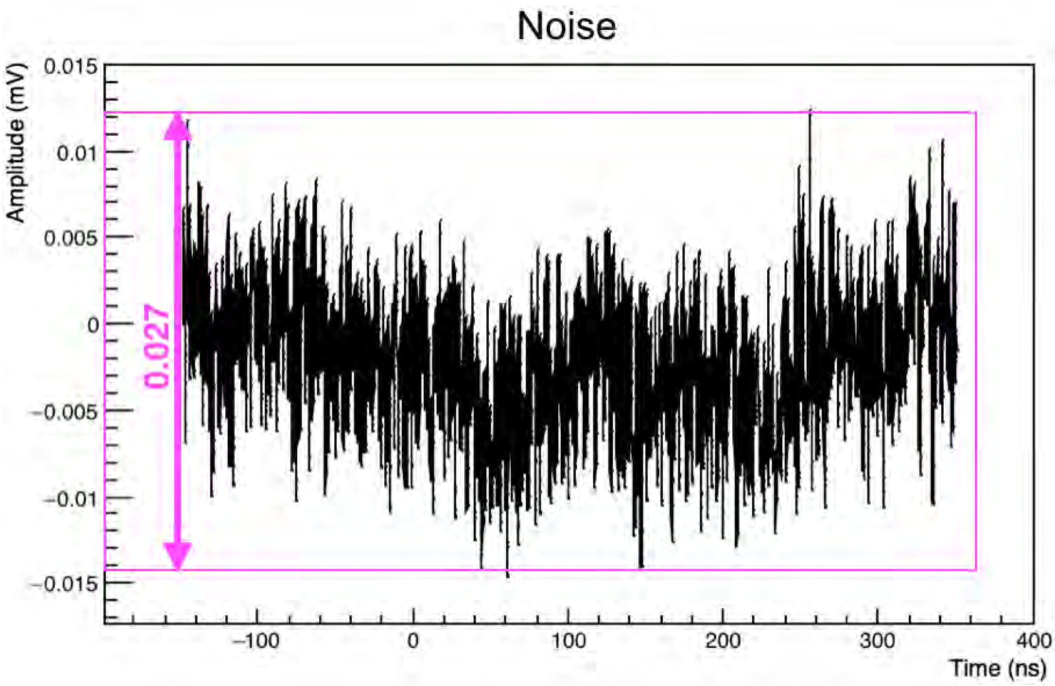


**Figure 3.4.** Typical noise trend observed among the oscilloscope signals. The maximum amplitude width is about 0.027 mV.

where $t_{low}$ and $t_{high}$ are the times at which the signal crosses the low and the high threshold, respectively.

The first step in the choice of the thresholds is the study of the typical noise associated with the detected signals, which is mainly due to the electronics. A series of triggered oscilloscope outputs has been reconstructed offline starting from raw data, and the results have been examined at times preceding the rising edge of the signals, to extrapolate the noise behaviour. As shown in Figure 3.4, the typical amplitude width associated to the electronic noise is $\sim 0.027$ mV. Therefore, values of $-0.1$ mV and $-0.03$ mV for the high and the low threshold respectively, and a time delay of $\Delta t \leqslant 10$ ns are a good choice, allowing to measure the arrival times at the very beginning of the rising edge of the signal, while assuring that only muon signals are considered.

### 3.2.2 Baseline correction

Inside of the laboratory there is a low frequency (few kHz) electromagnetic noise that biases the baseline of the fast GEM signal and can affect time resolution measurements. To estimate and correct this effect, the entire oscilloscope output has been reconstructed with a dedicated script. In Figure 3.5 an example of the result of this reconstruction is shown, obtained with the $ArCO_2$ gas

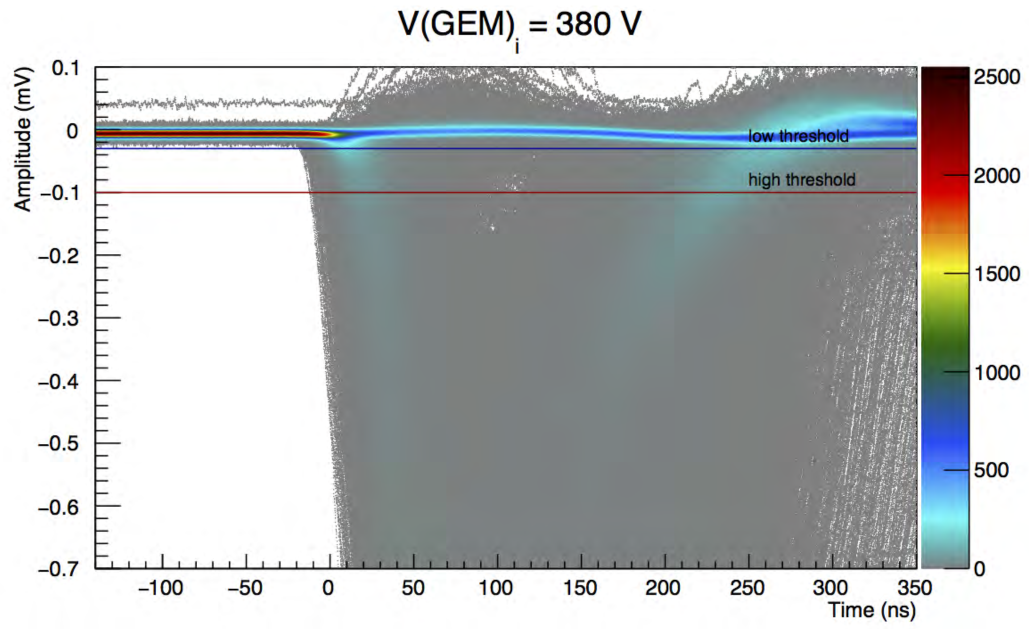


**Figure 3.5.** Reconstructed oscilloscope signals, obtained with the $Ar/CO_2$ gas mixture at $V(GEM)_i = 380$ V.

mixture at V(GEM)$_i$ = 380 V.

The correction consists of subtracting the calculated average baseline of each signal, $\bar{B}$, from the amplitude of each point of the recorded signal:

$$A_i^C = A_i - \bar{B} \; , \tag{3.1}$$

where $A_i$ and $A_i^C$ are the amplitudes of the point $i$ of a given signal before and after the baseline correction, respectively. To estimate the average baselines, the reconstructed output has been examined at times preceding the muon signals ($t \leqslant 50$ ns), in order to observe only the noise contribution. Under the assumption that the same noise affects all the measurement processes, this leads to

$$\bar{B} = \frac{\sum_i A_i}{N} \tag{3.2}$$

for a given signal, where N is the number of signal points in the region $t \leqslant 50$ ns.

The result of the baseline correction process over the entire set of signals shown in the aforementioned Figure 3.5, is reported in Figure 3.6. As expected, a noticeable improvement of the output can be observed, and similar refinements have been obtained for all the runs of both the gas mixtures.

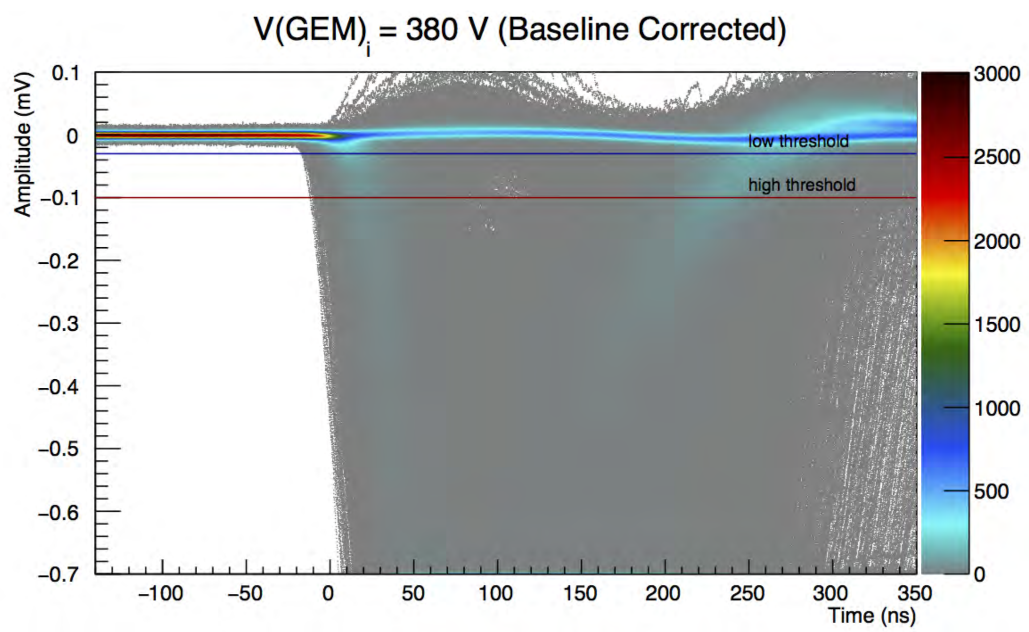


**Figure 3.6.** Result of the application of the Baseline Correction to the reconstructed oscilloscope signals, obtained with the $Ar/CO_2$ gas mixture at $V(GEM)_i = 380$ V.

### 3.2.3 Time resolution as a function of the voltage

After the application of the baseline correction, the time performance of the detector has been estimated from the distribution of the times at which the triggered, discriminated signals cross the low discriminator threshold. In fact, recalling Section 1.3, the width of this distribution is related to the intrinsic time resolution. This distribution should resemble a Gaussian curve, but may exhibit tails at low or high time values. The former may be due to the *bi-GEM* effect, while the latter may represent electrons that originate at the top of the drift region, and that need more time to cross the detector. These electrons, in fact, produce a signal closer in time to the firing of the bottom scintillator, with respect to the crossing times of the other electrons.

For these reasons, the Std[1] of the measured distribution can only give a rough estimate of the time resolution. A more precise result is provided by the sigma value obtained by fitting the distribution with a Gaussian curve, excluding the unwanted tails from the fit. In this case, the mean value of the fit provides the mean arrival time. Figure 3.7 shows the distribution obtained with the $Ar/CO_2/CF_4$ gas mixture at $V(GEM)_i = 470$ V and the corresponding fit.

Repeating the fitting procedure for all the voltage runs, for both the gas mix-

[1]Standard deviation

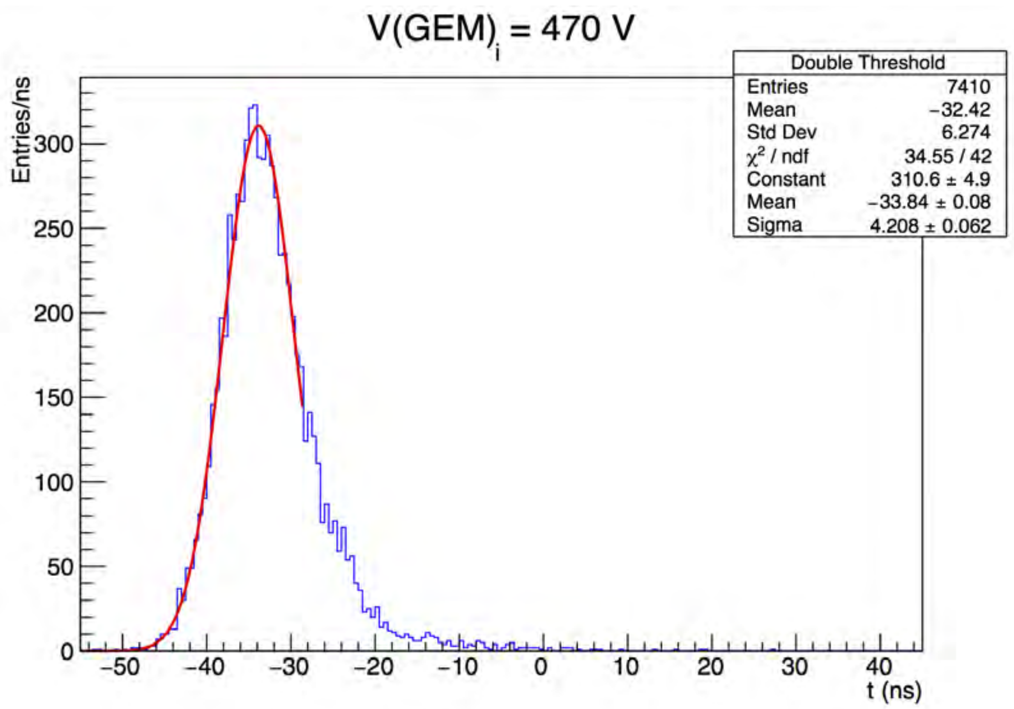


**Figure 3.7.** Distribution of the crossing times of the triggered signals, obtained with the $Ar/CO_2/CF_4$ gas mixture at $V(GEM)_i = 470$ V.

tures, the time resolutions as a function of the voltage applied to the GEM foils has been obtained, as reported in Figure 3.9 for $Ar/CO_2/CF_4$, and in Figure 3.9 for $Ar/CO_2$. As expected, in both cases the resolution estimate provided by the Std is significantly worse than that estimated by the Gaussian fit. The time resolution improves when a higher voltage is applied to the GEM foils, since higher voltages imply a higher number of primary ionizations (see Section 1.3). Moreover, the time resolution obtained for $Ar/CO_2/CF_4$ is better than that of $Ar/CO_2$, as expected since the $CF_4$ component has better time characteristics.

### 3.2.4 Detector efficiency

Since the two gas mixtures require different voltages to operate, in order to make a proper comparison between their time resolutions it is necessary to express them as a function of the detector efficiency, that is related to the gain. The efficiency of the GEM detector is given by the fraction of muons crossing it that is actually detected. This fraction corresponds to the number of triple coincidences, when both the scintillators and the GEM detector produce a signal within a given time interval, divided by the number of double coincidences, when the two scintillators fire but the GEM does not detect any signal. Before

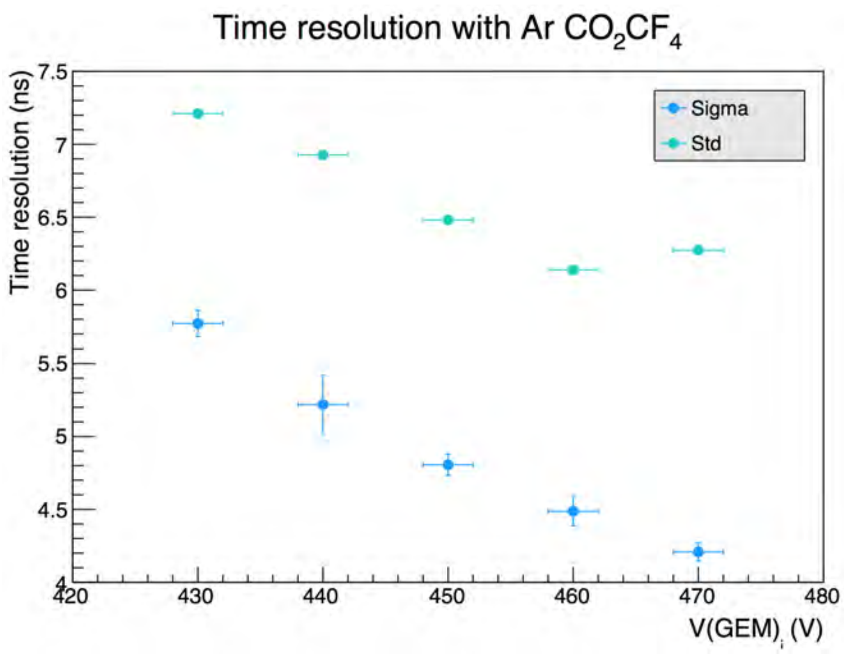


**Figure 3.8.** Time resolution as a function of the voltage difference applied between the two copper sides of the GEM foils, $V(GEM)_i$. A comparison between the standard deviation (Std) of the distribution of the arrival times, and the sigma obtained fitting the distribution with a Gaussian curve is shown. This result has been obtained with the $Ar/CO_2/CF_4$ gas mixture.

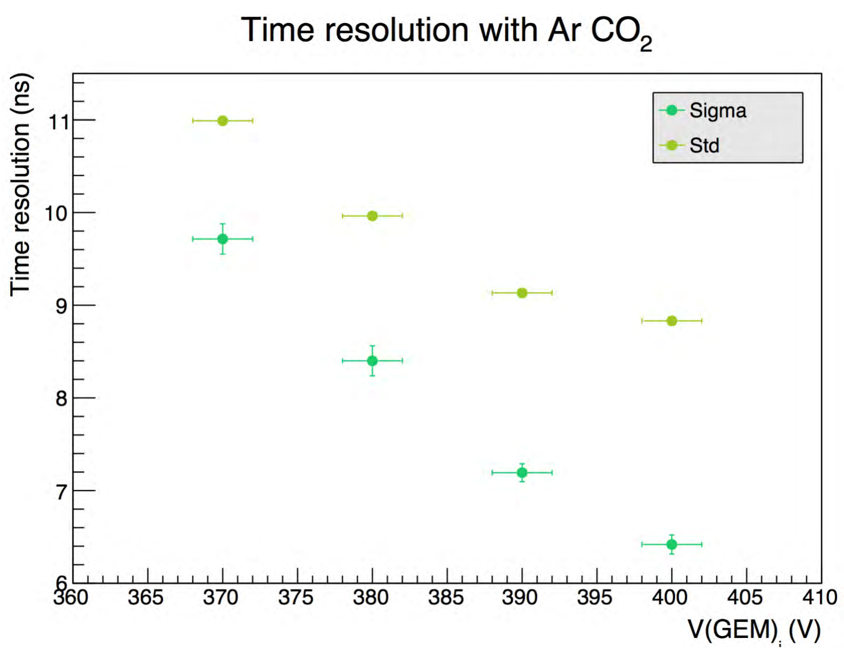


**Figure 3.9.** Time resolution as a function of the voltage difference applied between the two copper sides of the GEM foils, $V(GEM)_i$. A comparison between the standard deviation (Std) of the distribution of the arrival times, and the sigma obtained fitting the distribution with a Gaussian curve is shown. This result has been obtained with the $Ar/CO_2$ gas mixture.

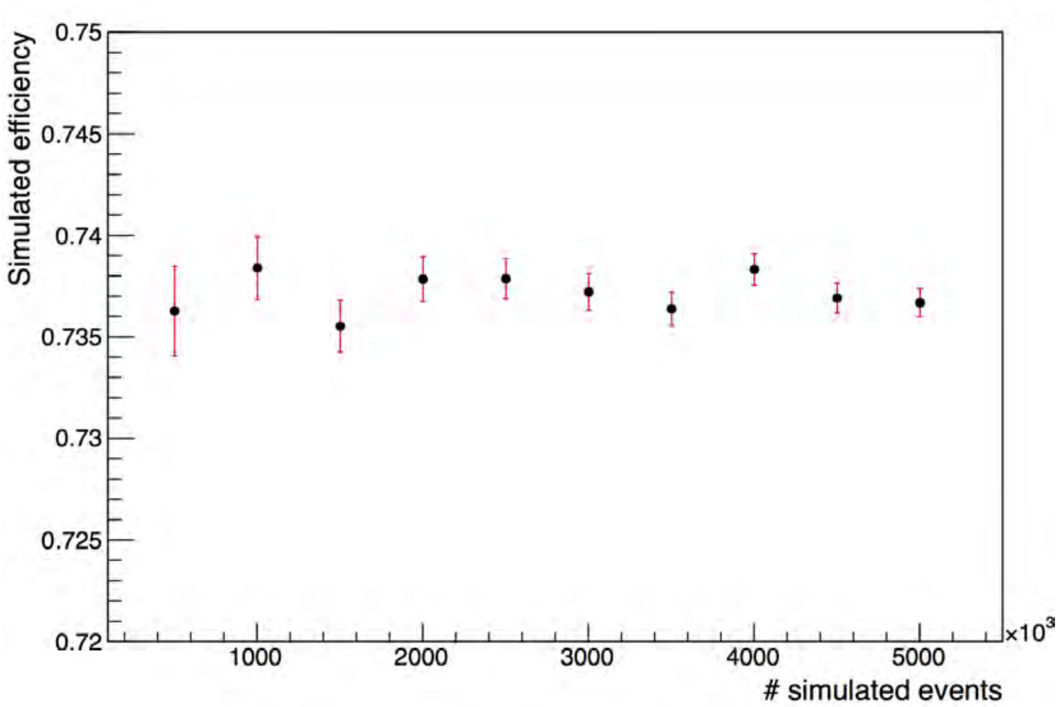


**Figure 3.10.** Simulated geometric efficiency as a function of the number of simulated muons, that ranges from $5 \times 10^5$ to $5 \times 10^6$.

measuring it, the geometric efficiency has been simulated using a *toy model* Monte Carlo script, specifically written for the experimental setup used. In this script the particular geometry of the system has been parametrized, as well as the angular distribution of the cosmic ray muon flux, that at the sea level exhibits a $\cos^2\theta$ behaviour, where $\theta$ is the zenith angle[2]. The geometric efficiency was calculated for an increasing number of simulated muons, from $5 \times 10^5$ to $5 \times 10^6$, with a pitch of 500. The result of the simulations as a function of the number of simulated muons is shown in Figure 3.10, and the efficiency values are reported in Table 3.1. As expected, the relative uncertainty on the calculated value, which has been estimated using Bayesian statistics, decreases with the number of muons, reaching values of less than 1%. The estimated efficiency has been compared to the measured values. From the experimental point of view of the present analysis, since a signal must pass the double threshold discriminator in order to be processed , the efficiency is measured as the number of discriminated signals divided by the total number of

[2]The dependence of the cosmic ray muon flux on the incident zenith angle can be expresses as $I(\theta, h, E) = I(0^\circ)\cos^{n(E,h)}(\theta)$, where $h$ in the vertical distance travelled by the muon, $E$ is the energy of the muon and $n(E, h)$ is an empirically determined constant. At the sea level, the experiments demonstrated that $n \sim 2$ [22].

**Table 3.1.** Simulated geometric efficiency as a function of the number of simulated muons. $\Delta$ (up) and $\Delta$ (down) are the uncertainties calculated using Bayesian statistics.

| Number of simulated muons | Efficiency | $\Delta$ (up) | $\Delta$ (down) |
|---|---|---|---|
| 50000 | 0.736274 | 0.002218 | 0.002229 |
| 100000 | 0.738393 | 0.001561 | 0.001567 |
| 150000 | 0.735522 | 0.001280 | 0.001284 |
| 200000 | 0.737837 | 0.001102 | 0.001104 |
| 250000 | 0.737861 | 0.000986 | 0.000988 |
| 300000 | 0.737211 | 0.000902 | 0.000904 |
| 350000 | 0.736381 | 0.000834 | 0.000836 |
| 400000 | 0.738319 | 0.000779 | 0.000780 |
| 450000 | 0.736908 | 0.000737 | 0.000738 |
| 500000 | 0.736679 | 0.000698 | 0.000699 |

triggered signals recorded. For each gas mixture, this ratio has been estimated for each value of the voltage applied to the GEM foils. The resulting efficiency plots as a function of the operating voltage are shown in Figure 3.11 and 3.12, for $ArCO_2CF_4$ and $ArCO_2$ respectively. There, the obtained curves have been fitted with the function

$$f(V(GEM)_i) = \frac{p_2}{1 + e^{p_0(V(GEM)_i + p_1)}} , \tag{3.3}$$

where $p_0$, $p_1$ and $p_2$ are free parameters. It is important to note that the measured values represent the overall efficiency, given by the product of the geometric efficiency, that depends only on the geometry of the system as in the simulated case, and of the intrinsic efficiency of the detector, that is a peculiar characteristic of the device itself. By looking at the plots, it is evident that the measured efficiency for $ArCO_2$ is $0.736 \pm 0.015$, compatible with the simulated values within the uncertainties, and leading to an intrinsic efficiency of $\sim 100\%$. The plateau value measured for $ArCO_2CF_4$ is instead $0.712 \pm 0.005$, slightly smaller than the simulated geometric efficiency. This may depend on the choice of the high threshold of the discriminator, that could be too stringent and cut a significant part of the real signals. On the other hand, tests performed with looser thresholds show an unexpected behaviour at high voltages, that may indicate the presence of discharges in the gas.

### 3.2.5 Time resolution as a function of the efficiency

The plots of the efficiency as a function of the operating voltage allowed to obtain a one-to-one correspondence between the $V(GEM)_i$ and efficiency values.

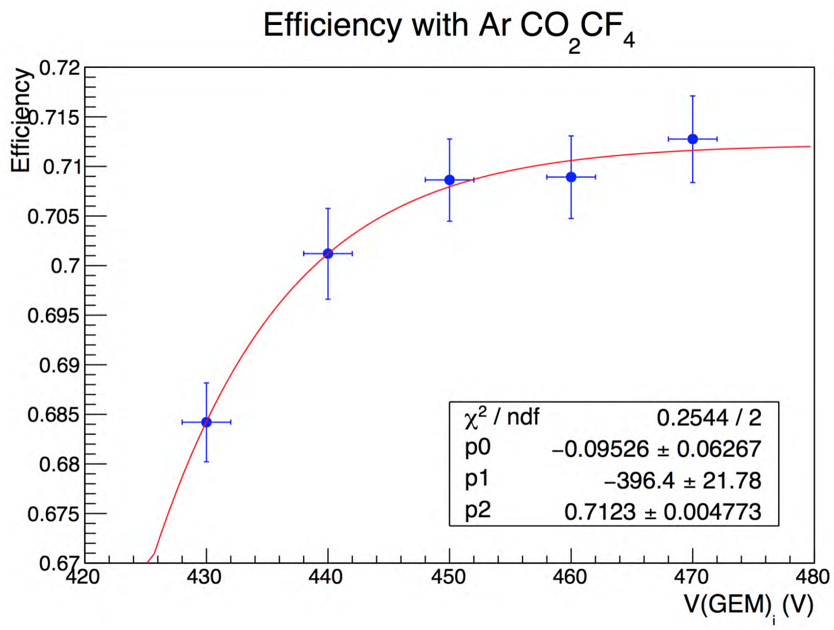


**Figure 3.11.** Detector efficiency as a function of the voltage difference applied between the two copper sides of the GEM foils, $V(\mathrm{GEM})_i$. This result has been obtained with the $Ar/CO_2/CF_4$ gas mixture.

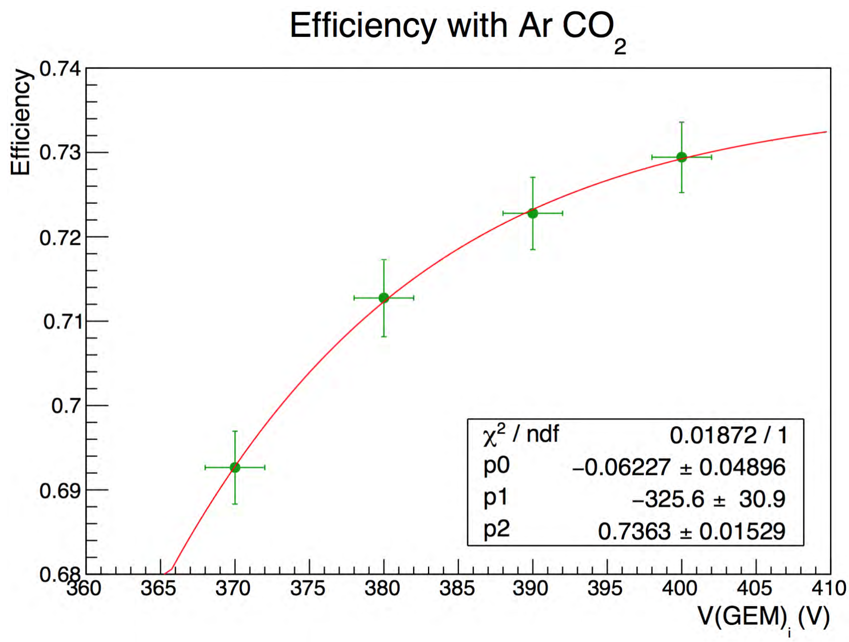


**Figure 3.12.** Detector efficiency as a function of the voltage difference applied between the two copper sides of the GEM foils, $V(\mathrm{GEM})_i$. This result has been obtained with the $Ar/CO_2$ gas mixture.

Therefore, it was possible to express the time resolution previously estimated for the two gas mixtures as a function of the measured efficiency. The results are shown in Figure 3.13. The time resolution obtained for $ArCO_2$ is of about 6.4 ns at the maximum measured efficiency. As expected, the addition of a small quantity of $CF_4$ to the mixture considerably improved this resolution, reaching values of around 4.2 ns, that are optimal for future upgrades of the CMS muon system.

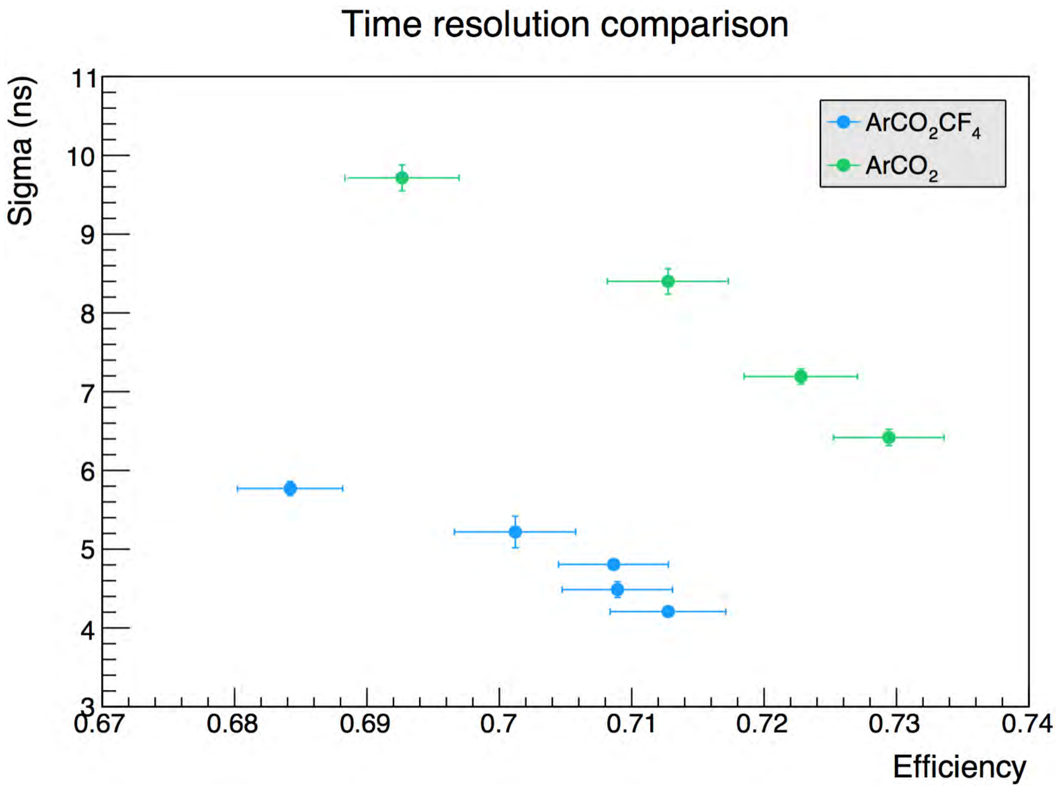


**Figure 3.13.** Time resolution as a function of the detection efficiency, showing a comparison of the results obtained with the $Ar/CO_2$ and the $Ar/CO_2CF_4$ gas mixtures.

# Summary and conclusions

The time performance of a triple-GEM detector has been studied by means of cosmic muon measurements, employing two different gas mixtures: $Ar/CO_2$ (70%/30%) and $Ar/CO_2CF_4$ (45%/15%/40%).

In order to appropriately compare the obtained results, the efficiency of the detector has been also measured, leading to an intrinsic efficiency of $\sim$ 100% for $Ar/CO_2$. Concerning the $Ar/CO_2CF_4$ mixture, the obtained efficiency reached a plateau at lower values with respect to the simulated geometric efficiency, implying an intrinsic efficiency lower than 100%. The inefficiency may depend on an overly-severe choice of the high discriminator threshold, even though tests performed with looser thresholds have shown unexpected behaviours at high voltages, maybe due to discharges through the GEM detector.

With the binary gas mixture $Ar/CO_2$ (70%/30%), the time resolution obtained by the Gaussian fit of the time distribution reaches values of about 6.4 ns. The addition of a fast component, $CF_4$, to the mixture improved the resolution up to about 4.2 ns for $Ar/CO_2CF_4$ (45%/15%/40%). These results make the triple-GEM detector a promising option for high-rate charged particle triggering, largely fulfilling the requirements for the CMS muon system, that must be satisfied in order to cope with the harsh environment expected in the future high luminosity phase of LHC.

# Bibliography

[1] F. Sauli, "Yellow report: Principles of operation of multiwire proportional and drift chambers", May 1977.

[2] M Alfonsi, G Bencivenni, P De Simone, F Murtas, M Poli-Lener, W Bonivento, A Cardini, C Deplano, D Pinci, D Raspino, and B Saitta, "Advances in fast multi-GEM based detector operation for high-rate charged-particle triggering", 2004.

[3] W Bonivento, G Bencivenni, G Felici, F Murtas, P Valente, A Cardini, A Lai, D Pinci, B Saitta, and C Bosio, "A triple GEM detector with pad readout for high rate charged particle triggering", *Nucl. instrum. methods phys. res., a*, vol. 488, no. 1-2, pp. 493–502, 2002.

[4] F. Sauli, "The gas electron multiplier (gem): Operating principles and applications", *Nuclear instruments and methods in physics research section a: Accelerators, spectrometers, detectors and associated equipment*, vol. 805, pp. 2 – 24, 2016, Special Issue in memory of Glenn F. Knoll, ISSN: 0168-9002. DOI: http://dx.doi.org/10.1016/j.nima.2015.07.060.

[5] S. Colafranceschi, "A study of materials used for muon chambers at the cms experiment at the lhc: Interaction with gas, new materials and new technologies for detector upgrade", Thesis, Feb. 2012.

[6] P. M. M. Correia, C. A. B. Oliveira, C. D. R. Azevedo, A. L. M. Silva, R. Veenhof, M. Varun Nemallapudi, and J. F.C. A. Veloso, "A dynamic method for charging-up calculations: the case of GEM", *Jinst*, vol. 9, P07025, 2014. DOI: 10.1088/1748-0221/9/07/P07025. arXiv: 1401.4009 [physics.ins-det].

[7] A Colaleo, A Safonov, A Sharma, and M Tytgat, "CMS Technical Design Report for the Muon Endcap GEM Upgrade", Tech. Rep. CERN-LHCC-2015-012. CMS-TDR-013, 2015.

[8] F. Sauli, "Gaseous Radiation Detectors", *Camb. monogr. part. phys. nucl. phys. cosmol.*, vol. 36, pp.1–497, 2014.

[9] Nov. 1998.

[10] P. R. B. Marinho, A. F. Barbosa, and G. P. Guedes, "Using a multilayer printed circuit board as position sensing electrode in a triple-gem detector", *Ieee transactions on nuclear science*, vol. 52, no. 6, pp. 2917 –2922, Jan. 2006.

[11] S. Chatrchyan *et al.*, "The CMS experiment at the CERN LHC", *Jinst*, vol. 3, S08004, 2008. DOI: 10.1088/1748-0221/3/08/S08004.

[12] G. L. Bayatian, S Chatrchyan, G Hmayakyan, *et al.*, *CMS Physics: Technical Design Report Volume 1: Detector Performance and Software*, ser. Technical Design Report CMS. Geneva: CERN, 2006, There is an error on cover due to a technical problem for some items.

[13] C. Collaboration, “CSC local efficiency measurements from run II data”, 2015.

[14] G. Abbiendi, “The CMS muon system in Run2: preparation, status and first results”, *Pos*, vol. EPS-HEP2015, p. 237, 2015. arXiv: 1510.05424 [physics.ins-det].

[15] S. Chatrchyan *et al.*, “The performance of the CMS muon detector in proton-proton collisions at sqrt(s) = 7 TeV at the LHC”, *Jinst*, vol. 8, P11002, 2013. DOI: 10.1088/1748-0221/8/11/P11002. arXiv: 1306.6905 [physics.ins-det].

[16] R Breedon and D Wenman, “Images of the CMS Muons - Cathode Strip Chambers (CSC)”, CMS Collection., 2008.

[17] K. Dong Hyun, “Work on CMS Muon Detector (RPC) during Long Shutdown 1 (LS1) - Point 5, Cessy, CMS cavern”, CMS Collection., 2015.

[18] J. Sturdy, “Overview of large-area gas electron multiplier detectors for the forward muon system of the CMS experiment at the high-luminosity LHC”, CERN, Geneva, Tech. Rep. CMS-CR-2016-047, 2016.

[19] D Contardo, M Klute, J Mans, L Silvestris, and J Butler, “Technical Proposal for the Phase-II Upgrade of the CMS Detector”, Geneva, Tech. Rep. CERN-LHCC-2015-010. LHCC-P-008. CMS-TDR-15-02, 2015.

[20] C. Caputo, “Physics Studies for the CMS muon system upgrade with triple-GEM detectors”, *Jinst*, vol. 9, no. 12, p. C12035, 2014. DOI: 10.1088/1748-0221/9/12/C12035.

[21] A. Balla *et al.*, “GASTONE: A new ASIC for the cylindrical GEM inner tracker of KLOE experiment at DAFNE”, *Nucl. instrum. meth.*, vol. A604, pp. 23–25, 2009. DOI: 10.1016/j.nima.2009.01.167.

[22] M. Bektasoglu and H. Arslan, “Investigation of the zenith angle dependence of cosmic-ray muons at sea level”, *Pramana*, vol. 80, pp. 837–846, 2013. DOI: 10.1007/s12043-013-0519-2.